Super Bound States in the Continuum on a Photonic Flatband: Concept, Experimental Realization, and Optical Trapping Demonstration

Ngoc Duc Le,[1,2] Paul Bouteyre,[1,3,*] Ali Kheir-Aldine,[1] Florian Dubois,[1,4] Sébastien Cueff,[1] Lotfi Berguiga,[1] Xavier Letartre,[1] Pierre Viktorovitch,[1] Taha Benyattou,[1] and Hai Son Nguyen[1,5,†]

[1]*Univ Lyon, ECL, INSA Lyon, CNRS, UCBL, CPE Lyon, INL UMR 5270, 69130 Écully, France*
[2]*Université Paris-Saclay, CNRS, CEA, Institut de Physique Théorique, 91191 Gif-sur-Yvette, France*
[3]*Department of Physics and Astronomy, University of Sheffield, S3 7RH, Sheffield, United Kingdom*
[4]*Silicon Austria Labs GmbH (SAL), 9524 Villach, Austria*
[5]*Institut Universitaire de France (IUF), 75231 Paris, France*

(Received 12 July 2023; accepted 18 March 2024; published 24 April 2024)

In this Letter, we theoretically propose and experimentally demonstrate the formation of a super bound state in a continuum (BIC) on a photonic crystal flat band. This unique state simultaneously exhibits an enhanced quality factor and near-zero group velocity across an extended region of the Brillouin zone. It is achieved at the topological transition when a symmetry-protected BIC pinned at $k = 0$ merges with two Friedrich-Wintgen quasi-BICs, which arise from the destructive interference between lossy photonic modes of opposite symmetries. As a proof of concept, we employ the ultraflat super BIC to demonstrate three-dimensional optical trapping of individual particles. Our findings present a novel approach to engineering both the real and imaginary components of photonic states on a subwavelength scale for innovative optoelectronic devices.

DOI: 10.1103/PhysRevLett.132.173802

Introduction.—In recent years, the photonic platform has advanced as a fertile research area for exploring non-Hermitian physics [1,2], where the interaction between the real (i.e., oscillation frequency) and imaginary (i.e., losses) components of photonic resonances can lead to unique phenomena that are absent in Hermitian systems. One archetypal object of non-Hermitian photonics is the "bound states in the continuum" (BICs) [3], which are perfectly confined modes despite lying in the continuum of radiating waves. These unique states are prevented from radiating due to either a symmetry mismatch with radiating waves in the case of "symmetry-protected BICs" (sym BICs), or through loss cancellation via destructive interference for "Friedrich-Wintgen BICs" (FW BICs) [4]. In a photonic lattice, each BIC is pinned at a singularity of far-field polarization vortex and possesses a "topological charge" determined by the corresponding winding number [5]. The topological nature of BICs has been explored by various research groups through numerous theoretical propositions [5–9] and experimental demonstrations [10–17]. However, most of these works only focus on manipulating the imaginary part of BIC modes, such as splitting BICs into lower-order BICs and chiral photonic states with circular polarization [6,15–17], or merging BICs to achieve "super BICs" characterized by a remarkably high quality factor over an extended region of the Brillouin zone [7,9,12,14,18].

In this Letter, we investigate the complex energy-momentum dispersion of photonic band structures when merging topological charges originated from a sym BIC at Γ point and two FW qBICs. Both BICs are located at photonic band edges of opposite curvature, and their merging gives rise to a super BIC sitting on an ultraflat band of zero curvature and infinite effective mass. All of the results obtained from numerical simulations are in good agreement with an analytical model based on mode coupling theory that nicely reproduces the real part of the band dispersion, the photonic quality factor and the corresponding far-field polarization texture. Transferring these concepts to real materials with technological constraints, the formation of flatband resulting from merging topological charges carried by BICs is experimentally demonstrated. Furthermore, we leverage this super BIC state to achieve the first experimental demonstration of optical trapping using BIC states. Our findings lay the groundwork for engineering photonic modes with robust quality factors and ultrahigh density of states, paving the way for innovative applications in lasing, particle trapping, and sensing.

Concept.—We start by considering a 1D photonic crystal slab having vertical symmetry $(-z \to z)$ and in-plane symmetry $(-x \to x)$ [Fig. 1(a)]. The structure has period $a = 330$ nm, total thickness $h = 350$ nm, and refractive index $n_{\mathrm{PC}} = 3.15$. We define the filling factor f as the proportion of one unit cell filled with air. To avoid any confusion, in this manuscript, we use the terms "odd" and "even" to describe the parity of the vertical symmetry, and the terms "symmetric" and "antisymmetric" for the parity of the in-plane symmetry. Figures 1(b) and (c) depict the

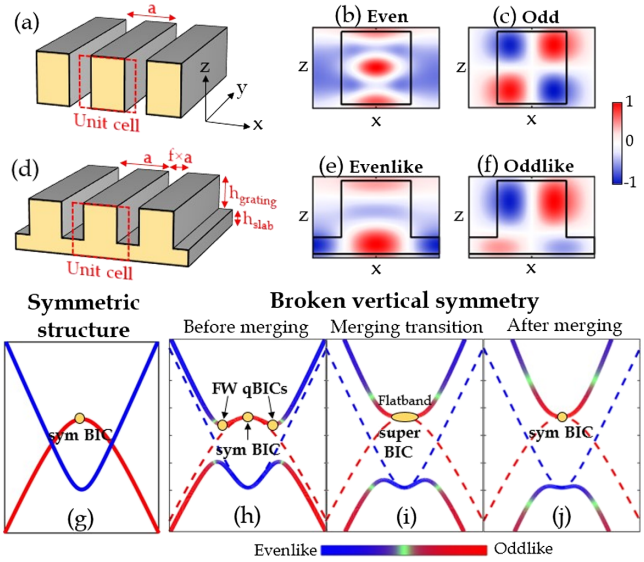

FIG. 1. (a) Sketch of 1D photonic crystal slab having vertical symmetry. Distribution of the electric field of (b) the even symmetric and (c) the odd antisymmetric modes of the TE polarization in the structure (a). (d) Sketch of 1D photonic crystal "comb" structure. Distribution of the electric field of (e) the evenlike symmetric and (f) the oddlike antisymmetric modes of the TE polarization in the structure (d). (g)–(j) The dispersion relations for $k_y = 0$ of (g) uncoupled even (blue) and odd (red) modes. (h) The coupling between oddlike and evenlike modes gives three BICs on a multivalley band. (i) The merging of the three BICs results in a super BIC on a flatband. (j) As the coupling coefficient α gets stronger, the band becomes parabolic.

profiles of the electric fields at the Γ point of the two lowest transverse-electric (TE) polarized modes, showing that the fundamental mode is even symmetric and the first excited mode is odd antisymmetric. Because of symmetry mismatch, these two modes are unable to couple with each other. Moreover, due to the symmetric parity, the fundamental mode is able to couple to the plane waves of the radiative continuum and becomes a leaky mode. By contrast, due to the antisymmetric parity, the first excited mode cannot couple to the radiative continuum, and forms a sym BIC at the Γ point [Fig. 1(g)].

Now, we break the vertical symmetry by implementing a thin unpatterned slab of thickness $h_{\text{slab}} = 80$ nm beneath the corrugated grating to create a "comb" structure. The height of the grating is $h_{\text{grating}} = 270$ nm. The fundamental and first excited modes are no longer even and odd and become evenlike symmetric [Fig. 1(e)] and oddlike antisymmetric [Fig. 1(f)], respectively. At the Γ point, the antisymmetric nature of the oddlike mode prevents it from coupling to the evenlike mode and the radiative continuum. Hence, it still exhibits a sym BIC at the Γ point. Out of the Γ point, the in-plane symmetry is broken, allowing the oddlike and evenlike modes to couple to each other. The coupling constant becomes stronger when we go further away from the Γ point, so we can approximate the coupling strength as $U = \alpha|k_x|$. Because this coupling mechanism involves the breaking of both the vertical and in-plane symmetries, we call it "symmetry-breaking coupling." This coupling mechanism is described by the Hamiltonian

$$H_{\text{comb}} = \begin{bmatrix} \omega_o & U \\ U & \omega_e \end{bmatrix} + i \begin{bmatrix} \gamma_o & \Gamma e^{-i\phi} \\ \Gamma e^{i\phi} & \gamma_e \end{bmatrix}. \quad (1)$$

Here, $\omega_{e(o)}(k_x, k_y)$ and $\gamma_{e(o)}(k_x, k_y)$ are the real and imaginary parts of the uncoupled even (odd) modes. The antidiagonal term Γ corresponds to the coupling rate between the two modes via the radiative channels. The phase shift ϕ is the relative dephasing when they radiate into the continuum. We focus on the case $k_y = 0$. The substantial hybridization between the evenlike and oddlike modes opens a gap at the anticrossing points of the dispersion curves, resulting in two bands of multivalley shape [Fig. 1(h)]. The loss exchange through the mode coupling mechanism reaches its peak when the Friedrich-Wintgen condition for destructive interference is satisfied: $\omega_o - \omega_e = \text{sign}(Z)\sqrt{[(W+V)/(W-V)]}(\gamma_o - \gamma_e)$ with $W = \sqrt{U^4 + 2U^2\Gamma^2\cos 2\phi + \Gamma^4}$, $V = U^2 - \Gamma^2$, and $Z = U\Gamma\cos\phi$. Therefore, one mode takes almost radiative loss and becomes a leaky mode, while the other mode experiences a minimal loss and becomes a FW qBIC localized near the anticrossing point.

As the coupling coefficient α gets stronger, the symmetry-breaking coupling intensifies through the whole reciprocal space, drawing the anticrossing points followed by the FW qBICs toward the Γ point. The coupling coefficient α can be controlled by varying the filling factor f [19]. This motion flattens the upper band. Therefore, an ultraflat band emerges when the BICs merge into a super BIC [12,14]. This super BIC has a large extension over a broad range of the dispersion curve. In other words, it is robust against oblique angles. Our work stands out from previous studies, which exclusively concentrated on the quality factor enhancement [7,12,14] or photonic flatbands focusing on density of states enhancement [18,23–29]. We introduce the concept of a "super bound state in the continuum on a flatband," referred to as an "ultraflat super BIC," which shows a dual effect: (i) quality factor enhancement due to the super BIC nature, and (ii) density of states enhancement resulting from the flatband characteristic.

Engineering the real part dispersion.—Figures 2(a)–2(c) display the reflectivity spectra of the "comb" structure for $k_y = 0$ for varying filling factor f, obtained using the numerical RCWA method [30]. These results reveal that before the merging transition [$f = 0.51$, Fig. 2(a)], a sym BIC and two FW qBICs coexist in the upper band, characterized by a multi-valley-shaped dispersion curve. At $f = 0.48$, the three BICs merge, forming a super BIC with an ultrasharp linewidth spanning a large portion of the Brillouin zone [Fig. 2(b)]. After the merging transition

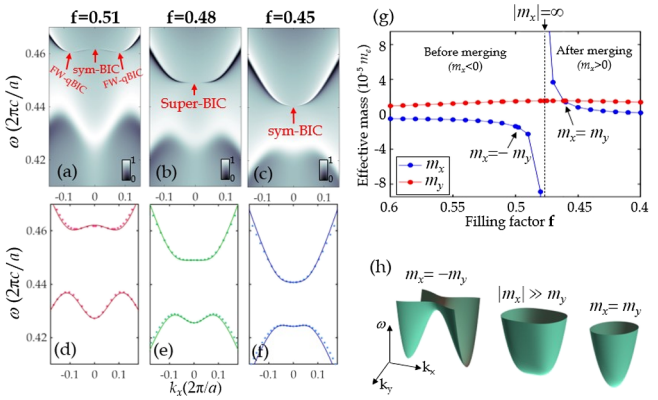

FIG. 2. (a)–(c) Numerical reflectivity spectra of the "comb" structure of filling factors $f = 0.51, 0.48, 0.45$, obtained by RCWA simulations ($k_y = 0$). (d)–(f) Comparison between the dispersion curves obtained from the RCWA simulations (dots) and from the analytical model (1) (solid line) for $k_y = 0$. (g) Effective masses m_x and m_y at the Γ point of the upper band as function of the filling factor f (RCWA simulations). (h) Dispersion surfaces correspond to the case of saddle surface ($f = 0.50$), ultraflat band ($f = 0.48$), and paraboloid surface ($f = 0.46$) (calculated using the COMSOL software).

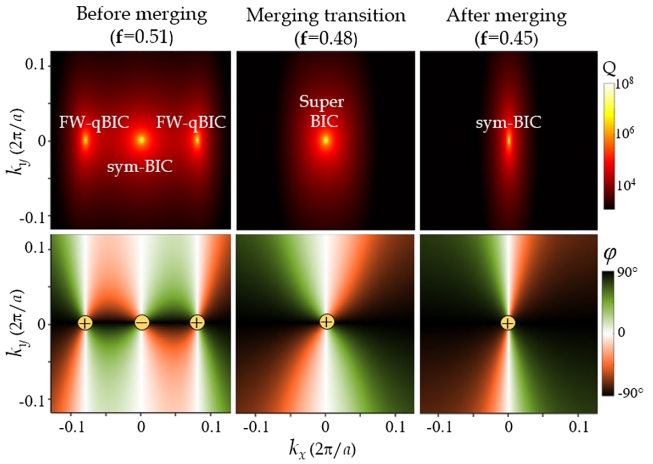

FIG. 3. First row: quality factor of the upper band as a function of k_x and k_y. Second row: orientation angle φ of the far-field polarization of the upper band. These results are obtained by using the analytical model based on the Friedrich-Wintgen formalism (1).

[$f = 0.45$, Fig. 2(c)], only the sym BIC remains. The RCWA results are accurately replicated by the analytical model based on the Friedrich-Wintgen coupling mechanism in (1) [19], with the results depicted by the solid lines in Figs. 2(d)–2(f). Concerning the dispersion characteristics along the k_y direction, they exhibit a simple parabolic dispersion of free particles with nearly constant positive curvature for all values of the filling factor f, since the corrugation is only along the x axis.

To summarize the dispersion properties along both k_x and k_y, Fig. 2(g) displays the photon effective masses m_x and m_y at the Γ point of the upper band. As previously mentioned, m_y remains almost constant with positive value as the filling factor f changes. Interestingly, m_x is negative before the merging transition, corresponding to the multivalley dispersion in Fig. 2(a). Its absolute value grows to infinity at the merging transition, indicating the presence of an ultraflat band, as shown in Fig. 2(b). After the merging transition, m_x becomes positive, corresponding to the parabolic dispersion with positive curvature in Fig. 2(c). Notably, $m_x = m_y$ at $f = 0.46$, where the dispersion relation is isotropic. Another special case occurs at $m_x = -m_y$ with $f = 0.50$. The dispersion surfaces of these configurations, as well as the ultra-flatband configuration, are illustrated in Fig. 2(h), depicting a transformation from a saddle surface to a paraboloid surface. It shows that isotropic dispersion surfaces can arise from such totally anisotropic configurations. These findings demonstrate that the "comb" structure can provide on-demand curvature in the momentum space.

Engineering the imaginary part and topological charges.—Figure 3 shows the mapping in momentum space of the quality factor and the orientation angle φ of the elliptic polarization of light. The results are obtained by using the analytical model (imaginary part for quality factor calculation, and eigenvectors for polarization texture) and are perfectly reproduced by numerical calculations (see Supplemental Material [19]). For the case $f = 0.51$, the figure clearly displays a sym BIC at the Γ point and two FW qBICs on the line $k_y = 0$. When $f = 0.48$, a super BIC emerges at the Γ point, exhibiting a large quality factor extension in momentum space as a result of the merging of the previously mentioned sym BIC and FW qBICs. At $f = 0.45$, only a sym BIC remains at the Γ point. These results are in perfect agreement with the calculated reflectivity spectrum previously presented in Fig. 2. The topological charge carried by each BIC is defined as the winding number of the far-field polarization vortex around this BIC [5] and is calculated from the orientation angle φ of the elliptic polarization

$$m = \frac{1}{2\pi} \oint_C d\mathbf{q} \cdot \nabla_{\mathbf{q}} \varphi \tag{2}$$

Our results show that each BIC carries a topological charge that equals to either $+1$ or -1. The sum of the topological charges is conserved, in agreement with previous works [7,12,14].

Experimental demonstration.—The concept of super BIC on flatband previously developed is adapted for amorphous silicon (a-Si) material (the spectral dependence of a-Si refractive index is shown in [19]). In our demonstration, the operating wavelength is targeted in the vicinity of 1 μm. Our sample consists of asymmetric a-Si gratings ($h_{\text{grating}} = 490$ nm, $h_{\text{slab}} = 100$ nm) on 2 μm of silica on silicon substrate [see Fig. 4(a)]. These structures (80 μm × 80 μm) were first defined in 300 nm thick hydrogen silsesquioxane resist layer by electron beam

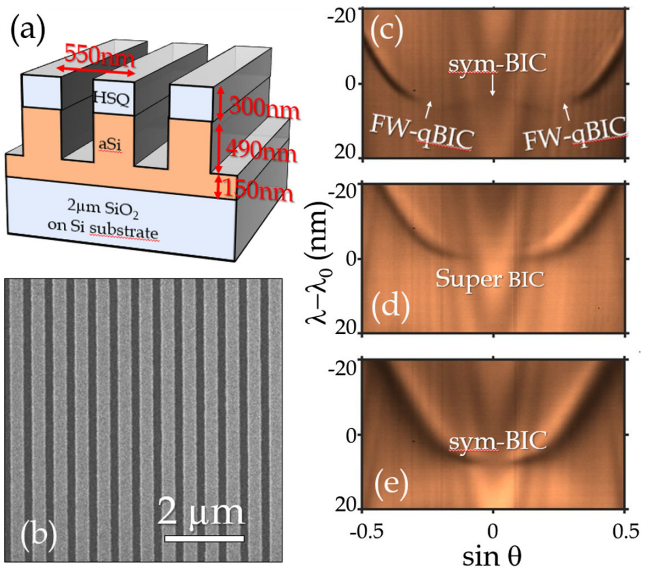

FIG. 4. (a) Sketch of the sample design. (b) SEM image of a grating structure (here $f = 0.39$). (c)–(e) Angle-resolved reflectivity measurements of three structures having three different filling factors f that correspond to (c) before merging, (d) at the merging transition, (e) after the merging transition. To follow the same photonic band, the spectral range of 40 nm is centered at $\lambda_0 = 1043$ nm (a), 1020 nm (b), 1007 nm (c).

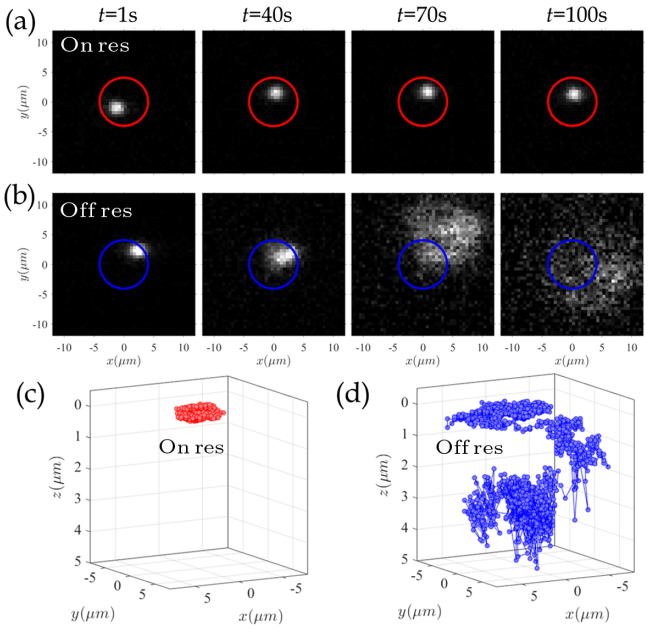

FIG. 5. (a),(b) Frames captured when the laser is on resonance (a), then off resonance (b) with the super BIC. The red (blue) circle corresponds to the laser spot at on (off) resonance with the super BIC. (c),(d) Coordinates of the particles extracted from the captured frames when the laser is on resonance (c), then off resonance (d) with the super BIC.

lithography, then were transferred subsequently to the a-Si layer via ionic dry etching (more details are reported in Supplemental Material [19]). All structures are of the same period of 550 nm but of different value for the filling factor f that varies from 0.35 to 0.65. Figure 4(b) represents the scanning electron microscopy (SEM) image of the structure corresponding to $f = 0.39$. A white light beam is focused onto the sample via a microscope objective (×50, NA = 0.65). The reflectivity is collected via the same microscope in a confocal geometry, and then projected in the Fourier space onto the entrance slit of a spectrometer. Finally, the signal is captured by the sensor of an infrared camera in the spectrometer output [19]. Figures 4(c)–(f) present angle-resolved reflectivity measurements of three structures of slightly different filling factor values. The spectral window has been chosen to monitor the transformation of the same photonic band from multivalley dispersion [Fig. 4(c)] to flatband [Fig. 4(d)] and then parabolic band [Fig. 4(f)]. We observe clearly the two FW qBICs at the valley points [Fig. 4(c)] and their merging with the sym BIC at the Γ point to form a super BIC [Fig. 4(d)]. All of these experimental results are in perfect agreement with the theoretical concepts shown in Figs. 1(h)–1(j) and then numerical and analytical results shown in Figs. 2(a)–2(f).

The ultraflat super BIC would find immediate use in various optoelectronic and optomechanic applications. Here, as an illustration, we will employ ultraflat super BIC for the first experimental demonstration of optical trapping assisted by photonic BIC. The combination of flatband and super BICs is the ideal configuration for optical trapping since (i) high group index and high photon effective mass are required for a practical realization of optical trapping [28], (ii) BICs exhibit strong field confinement to further improve the optical forces [31–33], with the possibility of tailoring novel trapping mechanisms enabled by BIC topological nature [32,34], and (iii) usually, nanotweezers rely on plasmonic [35] or dielectric cavities [36–38] that requires a nanometric position of the optical beam. In contrast, the robust quality factor and energy of the ultraflat super BIC against oblique wave vectors make this photonic mode a unique means for localizing photons of long lifetime under a resonant injection pump spot without photonic cavity. Therefore, one may induce trapping hot spots at any location of the structure via a resonant laser. Further discussions on the advantages of ultraflat super BIC for optical trapping are detailed in the Supplemental Material [19]. In our proof of concept, the particles that will be trapped are polystyrene beads of 1 μm size. These particles are diluted in water (10^7 beads/ml) that is kept in the fluidic reservoir of an optofluidic chamber. The sample, fixed to the wall of the fluidic reservoir from the inside and immersed in water, is excited by a tunable laser (1.25–1.6 μm) focused by a microscope objective (×20, NA = 0.4) to a 8.3 μm spot size. This corresponds to a converging beam with a full angle width of approximately 10° [19]. A fast camera is used to record a 200 s movie of two sequences: the laser wavelength is set on the resonance with the ultraflat super BIC for 100 s

[Fig. 5(a)], then set off resonance by 10 nm for the other 100 s half [Fig. 5(b)] (more frames are provided as videos in the Supplemental Material [19]). These results show that a single particle is trapped under the laser spot as soon as the laser is on resonance, and it will drift away as soon as the resonance is off. From the record frames, we can extract the x, y coordinates of the particle from the location of its center, and the z coordinate from its apparent diameter D when drifting out of focus, using $z = D\tan(\sin^{-1}\mathrm{NA})$. The extracted coordinates, shown in Figs. 5(a) and 5(b), clearly demonstrate a three-dimensional trapping of single particle with ultraflat super BIC. Further details and analysis on trapping mechanism with various BIC modes will be reported elsewhere.

Conclusion.—We introduce an original approach to engineer a new photonic state, the "ultraflat super BIC," by merging BICs located at band edges that exhibit opposite curvatures. Remarkably, the ultraflat super BIC exhibits a robust high quality factor and density of states over an extensive region of the momentum space. We successfully carried out the experimental demonstration using silicon gratings, where the full sequence of the merging transition was observed. Furthermore, we leveraged the ultraflat super BIC state for optical trapping, demonstrating three-dimensional trapping of single particles. Our results pave the way for exploring experimentally the topological forces texture associated with the topological charges of BICs [34]. We envision that the ultraflat super BIC holds potential for applications in low-threshold lasers [14,39] and highly sensitive sensors [40–42].

This work was partly funded by the French National Research Agency (ANR) under the project CELLDance (ANR-21-CE09-0011). We thank Patrice Genevet and Qinghua Song for fruitful discussions.

*N. D. L. and P. B. contributed equally to this letter as first authors.

†Corresponding author: hai-son.nguyen@ec-lyon.fr

[1] A. Guo, G. J. Salamo, D. Duchesne, R. Morandotti, M. Volatier-Ravat, V. Aimez, G. A. Siviloglou, and D. N. Christodoulides, Observation of $\mathcal{PT}$-symmetry breaking in complex optical potentials, Phys. Rev. Lett. **103**, 093902 (2009).

[2] C. E. Rüter, K. G. Makris, R. El-Ganainy, D. N. Christodoulides, M. Segev, and D. Kip, Observation of parity–time symmetry in optics, Nat. Phys. **6**, 192 (2010).

[3] C. W. Hsu, B. Zhen, A. D. Stone, J. D. Joannopoulos, and M. Soljačić, Bound states in the continuum, Nat. Rev. Mater. **1**, 16048 (2016).

[4] H. Friedrich and D. Wintgen, Interfering resonances and bound states in the continuum, Phys. Rev. A **32**, 3231 (1985).

[5] B. Zhen, C. W. Hsu, L. Lu, A. D. Stone, and M. Soljačić, Topological nature of optical bound states in the continuum, Phys. Rev. Lett. **113**, 257401 (2014).

[6] T. Yoda and M. Notomi, Generation and annihilation of topologically protected bound states in the continuum and circularly polarized states by symmetry breaking, Phys. Rev. Lett. **125**, 053902 (2020).

[7] M. Kang, S. Zhang, M. Xiao, and H. Xu, Merging bound states in the continuum at off-high symmetry points, Phys. Rev. Lett. **126**, 117402 (2021).

[8] M. Kang, L. Mao, S. Zhang, M. Xiao, H. Xu, and C. T. Chan, Merging bound states in the continuum by harnessing higher-order topological charges, Light Sci. Appl. **11**, 228 (2022).

[9] Q. Jiang, P. Hu, J. Wang, D. Han, and J. Zi, General bound states in the continuum in momentum space, Phys. Rev. Lett. **131**, 013801 (2023).

[10] Y. Zhang, A. Chen, W. Liu, C. W. Hsu, B. Wang, F. Guan, X. Liu, L. Shi, L. Lu, and J. Zi, Observation of polarization vortices in momentum space, Phys. Rev. Lett. **120**, 186103 (2018).

[11] H. M. Doeleman, F. Monticone, W. den Hollander, A. Alù, and A. F. Koenderink, Experimental observation of a polarization vortex at an optical bound state in the continuum, Nat. Photonics **12**, 397 (2018).

[12] J. Jin, X. Yin, L. Ni, M. Soljačić, B. Zhen, and C. Peng, Topologically enabled ultrahigh-q guided resonances robust to out-of-plane scattering, Nature (London) **574**, 501 (2019).

[13] X. Yin, J. Jin, M. Soljačić, C. Peng, and B. Zhen, Observation of topologically enabled unidirectional guided resonances, Nature (London) **580**, 467 (2020).

[14] M.-S. Hwang, H.-C. Lee, K.-H. Kim, K.-Y. Jeong, S.-H. K. Kwon, K. Koshelev, Y. Kivshar, and H.-G. Park, Ultralow-threshold laser using super-bound states in the continuum, Nat. Commun. **12**, 4135 (2021).

[15] W. Liu, B. Wang, Y. Zhang, J. Wang, M. Zhao, F. Guan, X. Liu, L. Shi, and J. Zi, Circularly polarized states spawning from bound states in the continuum, Phys. Rev. Lett. **123**, 116104 (2019).

[16] X. Zhang, Y. Liu, J. Han, Y. Kivshar, and Q. Song, Chiral emission from resonant metasurfaces, Science **377**, 1215 (2022).

[17] Y. Chen, H. Deng, X. Sha, W. Chen, R. Wang, Y.-H. Chen, D. Wu, J. Chu, Y. S. Kivshar, S. Xiao, and C.-W. Qiu, Observation of intrinsic chiral bound states in the continuum, Nature (London) **613**, 474 (2023).

[18] X. Letartre, S. Mazauric, S. Cueff, T. Benyattou, H. S. Nguyen, and P. Viktorovitch, Analytical non-Hermitian description of photonic crystals with arbitrary lateral and transverse symmetry, Phys. Rev. A **106**, 033510 (2022).

[19] See Supplemental Material at http://link.aps.org/supplemental/10.1103/PhysRevLett.132.173802 for details of (i) the theoretical models, (ii) sample fabrication, (iii) experimental setups, (iv) movie with more frames for the optical trapping, which includes Refs. [20–22].

[20] M. R. Dennis, Polarization singularities in paraxial vector fields: Morphology and statistics, Opt. Commun. **213**, 201 (2002).

[21] B. E. A. Saleh and M. C. Teich, *Fundamentals of Photonics*, 2nd ed. (John Wiley & Sons, Inc, Hoboken, New Jersey, 2007), p. 1201.

[22] E. Hecht, *Optics*, 5th ed. (John Wiley & Sons, Hoboken, New Jersey, 2017).
[23] H. S. Nguyen, F. Dubois, T. Deschamps, S. Cueff, A. Pardon, J. L. Leclercq, C. Seassal, X. Letartre, and P. Viktorovitch, Symmetry breaking in photonic crystals: On-demand dispersion from flatband to Dirac cones, Phys. Rev. Lett. **120**, 066102 (2018).
[24] S. Cueff, F. Dubois, M. S. R. Huang, D. Li, R. Zia, X. Letartre, P. Viktorovitch, and H. S. Nguyen, Tailoring the local density of optical states and directionality of light emission by symmetry breaking, IEEE J. Sel. Top. Quantum Electron. **25**, 1 (2019).
[25] H. Tang, F. Du, S. Carr, C. DeVault, O. Mello, and E. Mazur, Modeling the optical properties of twisted bilayer photonic crystals, Light Sci. Appl. **10**, 157 (2021).
[26] K. Dong, T. Zhang, J. Li, Q. Wang, F. Yang, Y. Rho, D. Wang, C. P. Grigoropoulos, J. Wu, and J. Yao, Flat bands in magic-angle bilayer photonic crystals at small twists, Phys. Rev. Lett. **126**, 223601 (2021).
[27] D. X. Nguyen, X. Letartre, E. Drouard, P. Viktorovitch, H. C. Nguyen, and H. S. Nguyen, Magic configurations in moiré superlattice of bilayer photonic crystals: Almost-perfect flatbands and unconventional localization, Phys. Rev. Res. **4**, L032031 (2022).
[28] N. Fayard, A. Bouscal, J. Berroir, A. Urvoy, T. Ray, S. Mahapatra, M. Kemiche, J. A. Levenson, J.-J. Greffet, K. Bencheikh, J. Laurat, and C. Sauvan, Asymmetric comb waveguide for strong interactions between atoms and light, Opt. Express **30**, 45093 (2022).
[29] Y. Yang, C. Roques-Carmes, S. E. Kooi, H. Tang, J. Beroz, E. Mazur, I. Kaminer, J. D. Joannopoulos, and M. Soljačić, Photonic flatband resonances for free-electron radiation, Nature (London) **613**, 42 (2023).
[30] M. G. Moharam, T. K. Gaylord, E. B. Grann, and D. A. Pommet, Formulation for stable and efficient implementation of the rigorous coupled-wave analysis of binary gratings, J. Opt. Soc. Am. A **12**, 1068 (1995).
[31] S. Yang, C. Hong, Y. Jiang, and J. C. Ndukaife, Nanoparticle trapping in a quasi-BIC system, ACS Photonics **8**, 1961 (2021).
[32] H. Qin, W. Redjem, and B. Kante, Tunable and enhanced optical force with bound state in the continuum, Opt. Lett. **47**, 1774 (2022).
[33] M. R. Hasan and O. G. Hellesø, Metasurface supporting quasi-bic for optical trapping and raman-spectroscopy of biological nanoparticles, Opt. Express **31**, 6782 (2023).
[34] H. Qin, Y. Shi, Z. Su, G. Wei, Z. Wang, X. Cheng, A. Q. Liu, P. Genevet, and Q. Song, Exploiting extraordinary topological optical forces at bound states in the continuum, Sci. Adv. **8**, 1961 (2022).
[35] H. M. K. Wong, M. Righini, J. C. Gates, P. G. R. Smith, V. Pruneri, and R. Quidant, On-a-chip surface plasmon tweezers, Appl. Phys. Lett. **99**, 061107 (2011).
[36] S. Mandal, X. Serey, and D. Erickson, Nanomanipulation using silicon photonic crystal resonators, Nano Lett. **10**, 99 (2010).
[37] L. Milord, E. Gerelli, C. Jamois, A. Harouri, C. Chevalier, P. Viktorovitch, X. Letartre, and T. Benyattou, Engineering of slow Bloch modes for optical trapping, Appl. Phys. Lett. **106**, 121110 (2015).
[38] R. Therisod, M. Tardif, P. R. Marcoux, E. Picard, J.-B. Jager, E. Hadji, D. Peyrade, and R. Houdré, Gram-type differentiation of bacteria with 2D hollow photonic crystal cavities, Appl. Phys. Lett. **113**, 111101 (2018).
[39] S. T. Ha, Y. H. Fu, N. K. Emani, Z. Pan, R. M. Bakker, R. Paniagua-Domínguez, and A. I. Kuznetsov, Directional lasing in resonant semiconductor nanoantenna arrays, Nat. Nanotechnol. **13**, 1042 (2018).
[40] F. Yesilkoy, E. R. Arvelo, Y. Jahani, M. Liu, A. Tittl, V. Cevher, Y. Kivshar, and H. Altug, Ultrasensitive hyperspectral imaging and biodetection enabled by dielectric metasurfaces, Nat. Photonics **13**, 390 (2019).
[41] D. N. Maksimov, V. S. Gerasimov, S. Romano, and S. P. Polyutov, Refractive index sensing with optical bound states in the continuum, Opt. Express **28**, 38907 (2020).
[42] H. Vyas and R. S. Hegde, Improved refractive-index sensing performance in medium contrast gratings by asymmetry engineering, Opt. Mater. Express **10**, 1616 (2020).